Instability Analysis of Sand under Undrained Biaxial Loading with Rigid and Flexible Boundary

Mousumi Mukherjee[1]; Anurag Gupta[2]; and Amit Prashant[3]

Abstract: The emergence of possible instability modes under undrained biaxial shear of sand was investigated to develop better understanding about the onset of localized and liquefaction-type solid-fluid instability modes using a generalized three-dimensional (3D) material model. These two modes are the primary instability modes that can exist in most cases while conducting undrained biaxial testing of sand at different densities, confining pressures, and boundary conditions. Using a 3D rate-independent and nonassociative constitutive model, the instability analysis was performed as a plane-strain bifurcation problem from a uniform stress-strain state. Large deformation formulation was used to simulate the biaxial test configuration with both rigid and flexible boundaries in the lateral direction. The existing theoretical framework of solid-fluid instability analysis under rigid boundaries was extended to the flexible lateral boundary condition. Interestingly, the onset of solid-fluid instability modes is significantly influenced by the choice of boundary conditions. The trends for the onset of various undrained instability modes were assessed as a function of material state variables. **DOI: 10.1061/(ASCE)GM.1943-5622.0000690.**

Author keywords: Plane strain; Sand; Bifurcation; Solid-fluid instability; Strain localization.

Introduction

Plastic instabilities in the form of bulging, surface buckling, volume or two-phase instability, and strain localization are often encountered during laboratory experiments of soil samples (Vardoulakis 1980; Desrues and Hammad 1989; Lade and Pradel 1990; Han and Vardoulakis 1991; Finno et al. 1996; Desrues and Viggiani 2004; Desrues and Georgopoulos 2006; Khoa et al. 2006; Daouadji et al. 2010). The deformation field of such samples bifurcates from an initial homogeneous to an inhomogeneous mode as a result of emergence of these plastic instabilities. The mode of instability depends on the type of loading, boundary and drainage conditions, along with the material properties (Vardoulakis 1981, 1985). Moreover, one instability mode can trigger the other, which subsequently leads to failure of the soil sample (Wan et al. 2013).

Liquefaction or flow sliding is a solid-fluid (SF) instability mode, which is generally encountered during undrained shearing experiments on loose sand (Lade 1992, 1993; Lade and Yamamuro 1997; Yamamuro and Lade 1997). Shear bands (localized zones of intense shearing) are another instability mode commonly observed in geomaterials that can result into catastrophic failure of complex geotechnical structures (Desrues et al. 1985). Although experimental investigations have primarily focused on strain localization in dense sands under drained conditions, recent studies have revealed that localization can take place in both loose and dense sands subjected to drained or undrained loading (Han and Vardoulakis 1991; Finno et al. 1996). In the case of loose saturated sand, undrained shear bands are of great concern because they can influence stability and postliquefaction deformation of earth structures. The localization phenomenon was observed to be more pronounced in biaxial tests compared to the true triaxial or axisymmetric triaxial test configuration (Desrues et al. 1985; Lade 2002; Alshibli et al. 2003). The shear stress ratio associated with the onset of static liquefaction also varied for these two types of tests (Wanatowski and Chu 2007; Chu and Wanatowski 2008).

Han and Vardoulakis (1991) carried out biaxial compression tests on water-saturated fine-grained St. Peter sandstone sand at different density states. In the case of axial load controlled tests, flow instability was noticed in loose and medium sand followed by shear band at large strain. On the other hand, diffused modes were observed in dense sand followed by localization and sometimes unstable pore pressure response. However, no localization was noticed in loose sands while performing undrained biaxial tests with controlled axial displacement. In these cases, diffused modes were found around peak and ultimate states. In displacement-controlled tests, shear bands emerged in medium and dense sands along with diffused modes at very large strain or prior to localization for the respective cases. Unlike drained tests with an isolated band, undrained shear bands emerged in conjugate periodic array, which further corresponded to dilatant and contractant material bands, indicating internal fluid flow to account for locally drained conditions. Similar to Han and Vardoulakis (1991), Desrues and Georgopoulos (2006), Khoa et al. (2006), and Daouadji et al. (2010, 2011) also observed nonlocalized diffused failure modes in the undrained displacement-controlled triaxial tests of loose sand along different stress paths. In contrast, Finno et al. (1996, 1997) and Mooney et al. (1997) noticed distinct shear bands in undrained strain-controlled biaxial compression tests of loose fine masonry sand. In these experiments, strain localization initiated in the form of temporary shear bands before mobilization of the peak friction angle, which finally formed a persistent shear band. The volume change within such a persistent shear band was not that significant. Mokni and Desrues (1998) performed a series of undrained biaxial tests on Hostun RF sand and observed strain localization in both loose and dense sand. In these experiments, localization in dense

[1]Ph.D. Scholar, Civil Engineering, Indian Institute of Technology Kanpur, Uttar Pradesh 208016, India. E-mail: mousumi@iitk.ac.in

[2]Associate Professor, Mechanical Engineering, Indian Institute of Technology Kanpur, Uttar Pradesh 208016, India. E-mail: ag@iitk.ac.in

[3]Associate Professor, Civil Engineering, Indian Institute of Technology Gandhinagar, Gujarat 382355, India (corresponding author). E-mail: ap@iitgn.ac.in

Note. This manuscript was submitted on August 31, 2015; approved on March 11, 2016; published online on April 26, 2016. Discussion period open until September 26, 2016; separate discussions must be submitted for individual papers. This paper is part of the ***International Journal of Geomechanics***, © ASCE, ISSN 1532-3641.

sand was associated with a cavitation phenomenon of pore fluid. It was concluded that the nondrainage condition impedes the localization phenomenon in dilative sand, and such cavitation was necessary to relax the isochoric constraint (no volume change) locally for allowing internal drainage in the sample.

Hill and Hutchinson (1975) presented a bifurcation-based theoretical study on different instability modes involved in plane-strain tensile testing of incompressible solids. The theoretical framework was modified by various researchers to incorporate compressive loading and extended to nonassociative, pressure-sensitive compressible media (Young 1976; Needleman 1979; Vardoulakis 1981; Chau and Rudnicki 1990). Vardoulakis (1985) further extended the plane-strain bifurcation analysis to water-saturated compressible media by taking into account the diffusion process. Row's dilatancy-based nonassociative flow rule was used therein to model the constitutive response of sand. SF and localized instability modes were identified for undrained plane-strain testing with rigid boundaries. Bardet and Shiv (1995) and Iai and Bardet (2001) modified the plane-strain bifurcation framework to account for general constitutive response and explored two-phase instabilities in hypoelastic and Mohr–Coulomb-type elastoplastic materials. More recently, Guo (2013) and Guo and Stolle (2013) followed a similar approach to explore undrained shear banding in sand. However, a better representation of the stress-strain relation is required to explain various instability modes that can emerge during undrained testing of sand at different stress states. For instance, a generalized pressure-dependent three-dimensional (3D) constitutive model with hardening is expected to predict instability behavior closer to the experimental observations. One of the objectives of this paper is to implement such a 3D material model and develop novel insights into the emergence of different undrained instability modes. Previously, Gajo et al. (2004, 2007) used a generalized 3D constitutive model and small deformation formulation to predict the localization onset and postlocalization behavior of sand in a drained biaxial test at varying initial densities and confining pressures. In a related study, Mukherjee et al., ("Emergence of drained instabilities in sand subjected to biaxial loading condition," submitted, *Comput. Geotech.*, Elsevier, Philadelphia) examined conditions for the onset of diffused and localized instability modes in drained biaxial testing of sand by implementing a similar 3D constitutive relation and large deformation framework. The background formulation used in this study is similar to Mukherjee et al., but with formulation and analysis focusing on SF instability and localization under undrained biaxial loading conditions. In addition, the existing basic formulation of the rigid boundary condition has been extended in the study to incorporate flexible lateral boundaries by deriving the necessary governing equations.

The instability analysis has been posed as a plane-strain bifurcation problem from a uniform stress-strain state. The undrained biaxial test configuration is simulated for both rigid and flexible boundaries in the lateral direction, which simulates displacement-controlled and stress-controlled loading, respectively. The material is assumed to follow a rate-independent framework of a generalized 3D nonassociative constitutive model. A large deformation formulation was used to investigate possible emergence of different bifurcated modes (i.e., SF or localized instabilities) at different states of material and boundary conditions. Trends for the onset of various undrained instability modes have been assessed further as a function of material state variables. One can analyze instability in other such boundary value problems by following a similar procedure or extending the solution to various numerical tools, such as the FEM. The main contributions of this paper are as follows:

- To explore possible instability modes that can emerge during undrained biaxial testing of sand at different densities, confining pressures, and boundary conditions. Implementation of a generalized pressure-dependent 3D constitutive model allows one to capture the emergence of two different undrained instability modes (i.e., SF and localized instabilities) under such different stress states that are consistent with previous experimental observations.
- The theoretical framework for plain-strain–based SF instability analysis has been extended to include flexible boundary conditions in addition to rigid ones. Interestingly, the onset of SF instability modes is significantly influenced by the choice of boundary conditions.

Plane-Strain Bifurcation Analysis

Problem Statement

A biaxially loaded rectangular saturated soil specimen of width $2L_1$ and height $2L_2$ (Fig. 1) is considered here with two types of lateral boundaries, flexible and rigid, while having a rigid boundary in the vertical direction. Shear stresses are assumed to be absent from all of the boundaries. Moreover, an undrained condition is imposed on these boundaries by ensuring no flow normal to the boundaries. In the first case with a flexible lateral boundary, as shown in Fig. 1(a), the top and bottom boundary ($x_2 = \pm L_2$) of the soil sample are given constant velocity in the x_2–direction, and the lateral surfaces are subjected to constant stress (σ_{11}). In

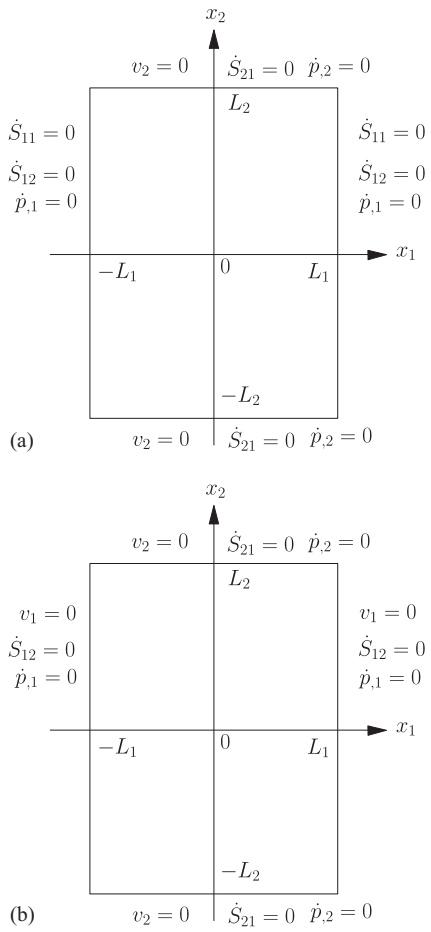

Fig. 1. Boundary conditions for plane-strain bifurcation under undrained loading with (a) flexible boundary and (b) rigid boundary

the second case with a rigid lateral boundary [i.e., in Fig. 1(b)], the sample is subjected to constant velocities in both x_1- and x_2-directions at boundaries $x_1 = \pm L_1$ and $x_2 = \pm L_2$, respectively. Although the stress-strain field initially remains homogeneous, with continued loading, an inhomogeneous stress-strain rate field may emanate as a result of bifurcation while satisfying the same equilibrium and boundary conditions. The bifurcation analysis aims to identify a nontrivial perturbed solution ($\mathbf{v}$) (i.e., the difference between the inhomogeneous and homogeneous velocity fields). The perturbed velocity field ($\mathbf{v}$) should satisfy the equilibrium and continuity equations along with the boundary conditions.

The equilibrium equations of the saturated sand sample under biaxial loading and in the absence of body force can be written in reference configuration as (Bardet 1991)

$$\begin{aligned} \dot{S}_{11,1} + \dot{S}_{21,2} &= 0 \\ \dot{S}_{12,1} + \dot{S}_{22,2} &= 0 \end{aligned} \tag{1}$$

where $\dot{S}$ = true rate of nominal stress tensor. If the current configuration is chosen as the reference configuration, $\dot{S}$ is related to the Jaumann rate of Kirchhoff stress ($\overset{\triangledown}{\boldsymbol{\tau}}$) through the Cauchy stress ($\boldsymbol{\sigma}$), rate of strain ($\mathbf{D}$), and spin tensor ($\mathbf{W}$), $\dot{\mathbf{S}} = \overset{\triangledown}{\boldsymbol{\tau}} - \boldsymbol{\sigma} \cdot \mathbf{W} - \mathbf{D} \cdot \boldsymbol{\sigma}$. In the case of no shear stress (i.e., $\sigma_{12} = \sigma_{21} = 0$), Eq. (1) then leads to

$$\begin{aligned} \overset{\triangledown}{\sigma}_{11,1} + \overset{\triangledown}{\sigma}_{21,2} - (\sigma_{11} - \sigma_{22})W_{12,2} &= 0 \\ \overset{\triangledown}{\sigma}_{12,1} + \overset{\triangledown}{\sigma}_{22,2} - (\sigma_{11} - \sigma_{22})W_{12,2} &= 0 \end{aligned} \tag{2}$$

Eq. (2) is written in terms of total stress tensors and can be related to the effective stresses by using Terzaghi's (1943) effective stress principle, $\sigma'_{ij} = \sigma_{ij} + p\delta_{ij}$, where σ_{ij}, σ'_{ij}, and p are the total Cauchy stress, effective Cauchy stress, and pore water pressure, respectively. The grain particles are assumed to be rigid in such effective stress principle (Terzaghi 1943). Notationally, dilation and stresses in tension are considered to be positive. The following relations can be obtained after substituting the effective stresses in Eq. (2):

$$\begin{aligned} \overset{\triangledown}{\sigma'}_{11,1} + \overset{\triangledown}{\sigma'}_{21,2} - (\sigma'_{11} - \sigma'_{22})W_{12,2} &= \dot{p}_{,1} \\ \overset{\triangledown}{\sigma'}_{12,1} + \overset{\triangledown}{\sigma'}_{22,2} - (\sigma'_{11} - \sigma'_{22})W_{12,2} &= \dot{p}_{,2} \end{aligned} \tag{3}$$

For isotropic material and incompressible pore fluid, the final form of equilibrium and continuity equations under plane-strain conditions can be written as (Vardoulakis 1985; Schrefler et al. 1990; Bardet and Shiv 1995; Iai and Bardet 2001)

$$\begin{aligned} d_1 v_{1,11} + d_3 v_{1,22} + (d_4 + d_7)v_{2,12} &= \dot{p}_{,1} \\ d_5 v_{2,11} + d_2 v_{2,22} + (d_4 + d_8)v_{1,12} &= \dot{p}_{,2} \\ \dot{p}_{,11} + \dot{p}_{,22} &= b(\dot{v}_{1,1} + \dot{v}_{2,2}) \end{aligned} \tag{4}$$

where
$d_1 = C_{1111} - \sigma'_{11}$; $d_2 = C_{2222} - \sigma'_{22}$; $d_3 = C_{1212} - 1/2(\sigma'_{11} - \sigma'_{22})$; $d_4 = C_{1212} - 1/2(\sigma'_{11} + \sigma'_{22})$; $d_5 = C_{1212} + 1/2(\sigma'_{11} - \sigma'_{22})$; $d_6 = C_{1212} + 1/2(\sigma'_{11} + \sigma'_{22})$; $d_7 = C_{1122}$; $d_8 = C_{2211}$, C_{ijkl} = elastoplastic tangent modulus defined in the subsequent section; $b = \gamma_w/\kappa$; and γ_w and κ = fluid unit weight and hydraulic permeability of the two-phase material, respectively. The perturbed velocity field should satisfy the following boundary conditions:

Case 1 (flexible lateral boundary)

$$\begin{aligned} &\dot{S}_{11} = d_1 v_{1,1} + d_7 v_{2,2} + \dot{p} = 0,\ \dot{S}_{12} = d_4 v_{1,2} + d_5 v_{2,1} = 0,\ \dot{p}_{,1} = 0 \quad \text{at} \quad x_1 = \pm L_1 \quad \text{and} - L_2 \le x_2 \le L_2 \\ &v_2 = 0,\ \dot{S}_{21} = d_3 v_{1,2} + d_4 v_{2,1} = 0,\ \dot{p}_{,2} = 0 \quad \text{at} \quad x_2 = \pm L_2 \quad \text{and} - L_1 \le x_1 \le L_1 \end{aligned} \tag{5}$$

Case 2 (rigid lateral boundary)

$$\begin{aligned} &v_1 = 0,\ \dot{S}_{12} = d_4 v_{1,2} + d_5 v_{2,1} = 0,\ \dot{p}_{,1} = 0 \quad \text{at} \quad x_1 = \pm L_1 \quad \text{and} - L_2 \le x_2 \le L_2 \\ &v_2 = 0,\ \dot{S}_{21} = d_3 v_{1,2} + d_4 v_{2,1} = 0,\ \dot{p}_{,2} = 0 \quad \text{at} \quad x_2 = \pm L_2 \quad \text{and} - L_1 \le x_1 \le L_1 \end{aligned} \tag{6}$$

Previous mathematical formulations for undrained instability analysis were developed under the assumption of a rigid boundary condition (Vardoulakis 1985; Bardet and Shiv 1995; Iai and Bardet 2001). The existing theoretical framework of SF instability analysis under rigid boundaries was extended here to incorporate flexible lateral boundary conditions. The equations for SF instability modes under flexible lateral boundaries are derived in Appendix I. These equations can be easily simplified to retrieve the conditions of SF instability under rigid boundaries (Appendix II), which were initially derived by Bardet and Shiv (1995). Another possible instability mode that can emerge under undrained biaxial loading with both types of lateral boundaries is the solid (S) instability mode in the form of localized shear bands. Although the undrained condition still prevails globally, internal local drainage is allowed at the emergence of such shear bands (Han and Vardoulakis 1991). Moreover, Guo (2013) showed an early initiation of shear band with an increase in permitted local volume change under globally undrained biaxial loading. In this study, the most critical case for localization was considered by analyzing it under locally drained conditions. The onset conditions for such modes are briefly discussed in Appendix III.

Material Model

The material behavior is characterized by an incremental elastoplastic constitutive relation

$$\overset{\triangledown}{\tau'}_{ij} = C_{ijkl} D_{kl} \tag{7}$$

where

$$C_{ijkl} = E_{ijkl} - \frac{E_{ijmn} P_{mn} Q_{rs} E_{rskl}}{H + Q_{ab} E_{abcd} P_{cd}} \tag{8}$$

E_{ijkl} is the isotropic elastic stiffness tensor given by

$$E_{ijkl} = G(\delta_{ik}\delta_{jl} + \delta_{ij}\delta_{kl}) + \lambda\delta_{ij}\delta_{kl} \tag{9}$$

where G and λ = Lame constants; δ_{ij} = Kronecker delta; H = hardening modulus; and $\mathbf{P}$ and $\mathbf{Q}$ = directions of outer normal to the plastic potential (g) and yield surface (f), respectively (i.e., $P_{ij} = \partial g/\partial \tau'_{ij}$ and $Q_{ij} = \partial f/\partial \tau'_{ij}$). Unlike the Mohr–Coulomb model, a generalized 3D constitutive model can account for evolution of the intermediate principal stress under plane-strain conditions. The 3D constitutive model proposed by Wood (2004) was used in this study. It is a nonassociative model based on a critical state concept that includes both shear and volumetric hardening and incorporates the effect of both density and confining pressure. The yield surface (f) and plastic potential (g) are defined by

$$f(\boldsymbol{\tau}', \varepsilon_q^p, \varepsilon_v^p) = \sqrt{3J_2} + \eta_y \frac{I'_1}{3} = 0 \tag{10}$$

$$g(\boldsymbol{\tau}') = \sqrt{3J_2} + M_c \frac{I'_1}{3} \ln \frac{3P'_r}{I'_1} \tag{11}$$

where ε_q^p and ε_v^p = shear and volumetric components of the logarithmic plastic strain tensor; I'_1 = first invariant of the Kirchhoff stress tensor; J_2 = second invariant of the deviatoric Kirchhoff stress tensor; M_c = slope of the critical state line in $\sqrt{3J_2}$ versus $(-I'_1/3)$ plane; P'_r = intercept of plastic potential on the $I'_1/3$ axis; and η_y = shear stress ratio $(-3\sqrt{3J_2}/I'_1)$, which is taken as a state variable and controls the evolution of the hardening modulus (H)

$$H = -\frac{\partial f}{\partial \eta_y} \frac{\partial \eta_y}{\partial \varepsilon_{ij}^p}^T \frac{\partial g}{\partial \tau'_{ij}} \tag{12}$$

Evolution of the η_y is related to accumulated plastic shear strain (ε_q^p) by the following hyperbolic function:

$$\frac{\eta_y}{\eta_p} = \frac{\varepsilon_q^p}{a + \varepsilon_q^p} \tag{13}$$

where a = constant; and η_p = peak shear stress ratio. Here, η_p is defined as a function of another state variable (ψ), which includes information on density or specific volume and mean stress

$$\eta_p = M_c - \kappa\psi = M_c - \kappa v - \Gamma + \Lambda_c \ln(-I'_1/3) \tag{14}$$

where κ = material constant; Λ_c = slope of the critical state line in the compression plane; and Γ = intercept of the critical state line on the specific volume axis at a mean pressure level of 1 kPa.

Undrained Biaxial Test Simulations

Undrained biaxial tests were simulated for sand samples (Hostun RF sand) at different density states with initial void ratios (e_0) varying from 0.65 to 0.85 and initial effective confining pressures ranging from 100 to 400 kPa. The material parameter values used in the simulation are listed in Table 1. There exist many expressions in the literature that consider the influence of mean pressure on the elastic stiffness of soil (Desai and Siriwardane 1984; Lade and Nelson 1987; Hicher 1996; Houlsby et al. 2005; Einav and Puzrin 2004). Following Gajo and Wood (1999), a pressure-dependent elastic tangent stiffness was used in the analysis. In this case, the elastic shear modulus (μ) is related to the dynamic shear modulus (G_0) through a scalar factor, where G_0 is a function of the initial specific volume (v_0) and the mean effective stress ($I'_1/3$) is expressed in kilopascals (Hardin and Black 1966)

Table 1. Material Constants Considered in Analysis (Data from Gajo and Wood 1999 and Wood 2004)

Parameter	Description	Value
G	Shear modulus	$G_0/3$
ν	Poisson's ratio	0.1
M_c	Slope of critical state line in $\sqrt{(3J_2)}$–$(-I'_1/3)$ plane	1.2
Λ_c	Slope of critical state line in specific volume (v)-ln $(-I'_1/3)$ plane	0.03
Γ	Intercept for critical state line in v-ln $(-I'_1/3)$ plane at 1 kPa effective mean pressure	1.969
a	Parameter controlling hyperbolic stiffness relationship	0.0016
κ	Relation between changes in state parameter (ψ) and current peak stress ratio (η_p)	2

Table 2. Critical Void Ratio at Different Initial Effective Confining Pressures

Initial effective confining pressure (kPa)	Critical void ratio (e_c)
100	0.83
200	0.81
300	0.798
400	0.789

$$G_0 = 3230 \frac{(3.97 - v_0)^2}{v_0} \sqrt{-I'_1/3} \tag{15}$$

The homogeneous stress-strain field for the undrained biaxial test was obtained by numerically integrating the elastoplastic constitutive Eqs. (8)–(14) using a fully explicit return mapping algorithm (Simo and Hughes 2000) subjected to the boundary conditions [Eqs. (5) and (6)]. An objective algorithm based on the notion of rotated configuration was used for such large deformation simulations along with the explicit return mapping scheme (Dodds and Healy 2001). The plane-strain biaxial stretching, however, does not involve any rotation until the emergence of any types of instability. Hence, for such a case, the unrotated and the Jaumann rate of Cauchy stress become identical for the homogeneous stress-strain field.

The sand samples are identified to be at loose or dense state depending on the critical void ratio (e_c) at any confining pressure, which is calculated using Eq. (16), and its values are listed in Table 2

$$(1 + e_c) - \Gamma + \Lambda_c \ln(-I'_1/3) = 0 \tag{16}$$

Typical stress-strain behavior, pore pressure response, and stress paths are plotted in Fig. 2 at two density states, with $e_0 = 0.65$ and 0.85, and initial effective confining pressure varying from 100 to 400 kPa. For the dense sample ($e_0 = 0.65$), where the void ratio is lower than the critical void ratio, shear stresses were observed to increase continuously with increased shearing, whereas for the loose sample ($e_0 = 0.85$) with a void ratio higher than the critical value, shear stresses started to decrease after exhibiting a distinct

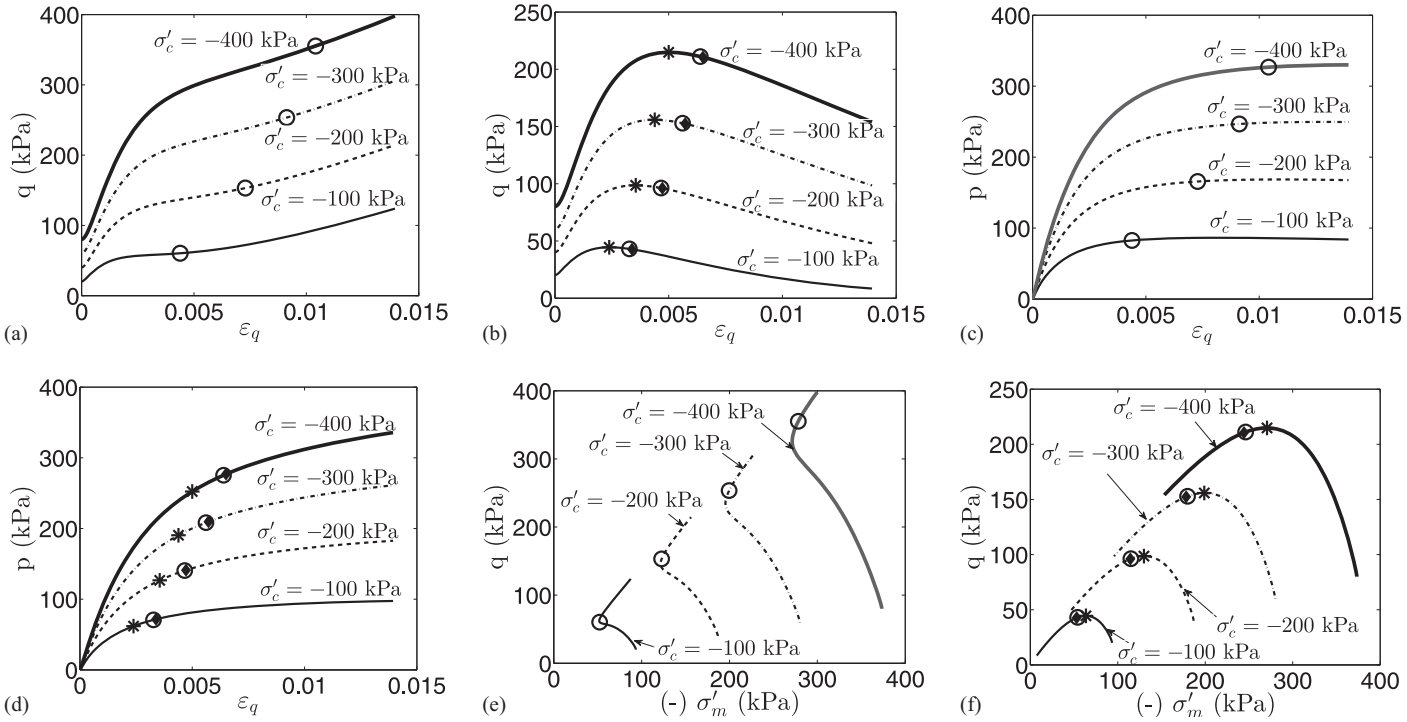

Fig. 2. Evolution of (a and b) stress-strain, (c and d) pore pressure, and (e and f) stress-path behavior for $e_0 = 0.65$ and 0.85 with varying initial effective confining pressures (σ'_c) (Note: q, σ'_m, p, and ε_q are the shear stress, effective mean pressure, pore pressure, and shear strain, respectively)

peak, irrespective of the level of confining pressure. The continued shearing of loose sand showed an increasing trend in the pore pressure response, confirming a contractive volumetric behavior. In contrast, the dense sand showed an initial increase and then a gradual decrease in pore pressure, indicating an overall dilative volumetric response. The variation of pore pressure also affected the mean effective stress during shearing, which is presented in the stress-path plots of Figs. 2(e and f). Fig. 3 presents the stress-strain behavior and the associated stress paths of undrained biaxial loading on sand at various void ratios for two initial effective confining pressures, 100 and 400 kPa. The trend in stress-strain response and stress-path behavior at these two confining pressures remained unchanged for dense and loose sands. However, in the case of medium to dense sand ($e_0 = 0.7$), the level of confinement had a significant influence on the nature of stress-strain and stress-path behavior. At a lower confining pressure (100 kPa), a temporary decrease of shear stress was noticed after the initial peak, which was followed by a sharp change in phase with a persistent increase in the shear stress. In contrast, at a higher confinement (300 kPa), the shear stress exhibited a continuously increasing trend accompanying reduction in pore pressure. The simulated stress-strain and pore pressure response was qualitatively in good comparison with the behavior reported in various triaxial or biaxial experiments of sand samples (Han and Vardoulakis 1991; Finno et al. 1997).

Instability under Various Boundary Conditions

The emergence of possible instability modes (i.e., two-phase and localization instabilities) was investigated under the boundary conditions given in Eqs. (5) and (6) for the undrained simulations presented in the previous section of a biaxial sample with an aspect ratio (L_2/L_1) of 2. Because most of the instabilities were found at the small strain level, results from large deformation simulations were not very different from the small deformation analysis and are not presented here separately. These instability modes were assumed to develop from a homogeneous stress-strain field, which was valid until the emergence of any instability. Hence, this analysis only predicts the onset of each of these possible types of instability modes and does not include identification of gradually evolving multiple instability modes on continued shearing under the given test conditions.

The instability onsets are determined here based on Hill's (1958, 1961) global stability framework, where localization is captured from the loss of the ellipticity condition of the differential equation governing the local rate equilibrium. Bigoni and Hueckel (1991) and Bigoni (2000) proposed several local stability criteria to predict the instability onset for nonassociative material; these criteria are derived from the positiveness of second-order work. The global criteria of bifurcation can also be used to derive these local criteria, and the condition for localization under these two frameworks is essentially the same (Bigoni 2000). Vardoulakis (1996a, b) used a similar local stability approach for exploring the undrained instabilities for biaxial loading on sand. Recently, Borja (2006) analyzed liquefaction-type undrained instabilities under a general 3D loading condition based on the local stability and uniqueness criterion. In this case, instability modes do not depend on the flow boundary condition; rather, the continuity equation was imposed as a constraint on the stability modes. However, the present analysis is based on the global stability criteria, which were previously followed by Hill and Hutchinson (1975), Bardet (1991), Vardoulakis (1985), and Bardet and Shiv (1995).

Two-Phase Instability Modes under Rigid Boundary

Two-phase or SF instability modes in the rigid boundary were identified by checking against the condition [Eq. (31)] from

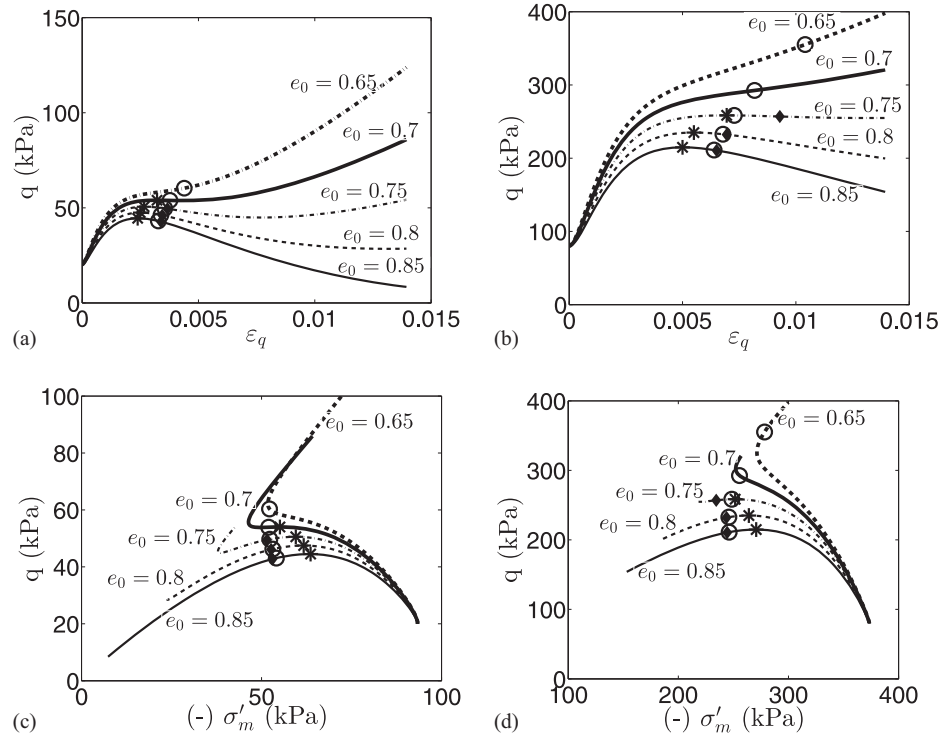

Fig. 3. Evolution of (a and b) stress-strain and (c and d) stress-path behavior for $\sigma'_c = -100$ and –400 kPa with varying void ratios (Note: q, σ'_m, and ε_q are the shear stress, effective mean pressure, and shear strain, respectively)

Appendix II. Fig. 4 presents the evolution of the undrained instability parameter (b^2-4c) of Eq. (31) during shearing for a void ratio of 0.7 at initial effective confining pressures of 100 and 400 kPa. The two-phase instability condition was observed to get satisfied for the case with 100-kPa confining pressure. The wavelength ratio ($\Lambda = \beta_1/\beta_2 = \pm 1$) was obtained at the onset of two-phase instability, which also corresponds to the case of $m_1/m_2 = L_1/L_2 = 1/2$.

The onset of SF instability modes at various void ratios and confinement was calculated and is marked in Figs. 2 and 3. Such modes emerged just before the peak shear stress for sands with loose and medium-density states. Hence, undrained strain softening is generally associated with SF instability modes, which is also termed as static liquefaction phenomenon. These modes were observed to be delayed with decreasing void ratio and an increase in the initial effective confining pressure. In the case of medium-dense sand, two-phase instability modes were activated only at lower confinements with a clear phase change.

Two-Phase Instability Modes under Flexible Boundary

The onset of SF instability under the flexible lateral boundary was analyzed for the first time theoretically. Two-phase instability modes for the flexible boundary were investigated by checking against the condition $\bar{G} = 0$ from Eq. (26). Solutions were obtained for the fundamental mode ($m_1 = 1$ and $m_2 = 2$), which was observed to be the critical mode in the rigid boundary case. Because the expression $\bar{G}$ is undefined at $x_1 = 0$, the expression $\lim_{x_1 \to 0} \bar{G}$ for this mode was evaluated near the point with $x_1 = 0$

$$\bar{G}_{0+} = \lim_{x_1 \to 0} \bar{G} = (2d_4 + d_7 + d_8 - d_1 - d_2)\,\gamma_1 2\beta_2 2 - d_3\beta_2 4 - d_5\gamma_1 4 \tag{17}$$

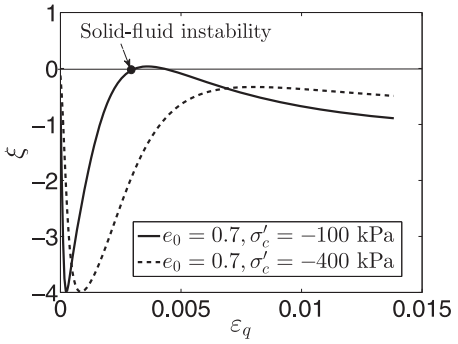

Fig. 4. Evolution of undrained instability parameter ($\xi = b^2 - 4c$) for void ratio 0.7 at initial effective confining pressures 100 and 400 kPa

The expression in Eq. (17) is very similar to the condition $G_r = 0$ of the rigid boundary case; however, β_1 is replaced here with γ_1, and an additional constraint of Eq. (22) needs to be satisfied. The expression of $\bar{G}_{0+}$ was observed first to satisfy the condition $\bar{G} = 0$ compared to the other values of x_1, implying that the two-phase instability initiates around a point with $x_1 = 0$. Iai and Bardet (2001) also showed the vortex of the perturbed velocity field for this mode ($m_1 = 1$ and $m_2 = 2$) to lie on the x_2-axis. The evolution of $\bar{G}_{0+}$ for the simulation of the $e_0 = 0.85$ sample at an initial effective confining pressure of 100 kPa has been plotted in Fig. 5. SF instability mode was identified when $\bar{G}_{0+}$ changed its sign from negative to positive. Two-phase instabilities for other simulations in the flexible condition were also determined and have been marked in Figs. 2 and 3. In the flexible case, a general trend of delayed onset for two-phase instability was observed in comparison to the rigid boundary condition. Unlike in the rigid boundary, no SF instability was observed for

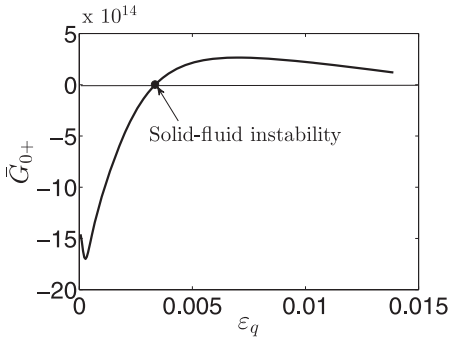

Fig. 5. Evolution of undrained instability parameter in flexible boundary ($\bar{G}_{0+}$) for void ratio 0.85 at initial effective confining pressure 100 kPa

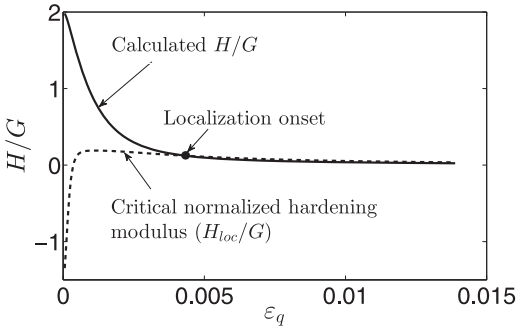

Fig. 6. Evolution of actual and critical normalized hardening modulus for undrained biaxial test with void ratio 0.65 and initial effective confining pressure of 100 kPa

the medium-dense sand with a void ratio of 0.7 under a 100-kPa initial effective confining pressure. Similar to the rigid case, two-phase instability in the flexible boundary was also precluded with an increase in level of confinement and decreasing void ratio. Because the SF instability mode is more critical in the rigid lateral boundary case, from here on, these modes will be discussed specifically in reference to the rigid boundaries only. SF modes were important to analyze in the flexible case to explore the possibility of such modes appearing before localization phenomena, which is further discussed in the subsequent section.

Localized Modes

The localization onsets for different biaxial test simulations were captured using the conditions $N = 0$ or $\bar{N} = 0$ as discussed in Appendix III. For each of such biaxial loading configurations, a critical hardening modulus (H_{loc}) was calculated at every stress state for satisfying the requirement of localization on the elliptic/hyperbolic boundary. The localization mode was triggered only when the critical hardening modulus could exceed the actual hardening modulus at any stress state. The evolution of the critical hardening modulus, normalized by the elastic shear modulus (G), is plotted in Fig. 6 for the sand sample at $e_0 = 0.65$ and 100 kPa initial effective confining pressure. For this case, the localization took place at approximately 0.45% shear strain. Localization onsets for other biaxial simulations were identified in a similar manner and have been marked in Figs. 2 and 3. Such modes for rigid boundaries were more prevalent for the dense sand than the loose or medium-dense sands, where localized modes were preceded by the SF instability mode. However, localized modes emerged first in the flexible boundary case, followed by the two-phase instability modes in the case of loose-sand samples. Finno et al. (1997) and Mooney et al. (1997) also noticed that the localized modes initiate from the uniform deformation field under biaxial loading with flexible lateral boundaries, compared to the two-phase or liquefaction-type modes. Similar to the two-phase modes, localization behavior was also retarded by an increase in the level of confinement, resulting in a higher onset shear strain at localization. However, for medium-dense sand, an increase in confinement changed the instability type from a two-phase to a localized one. Implementation of the generalized constitutive relation with the 3D hardening rule allows one to capture such a change in the instability behavior of the sand sample. Fig. 7(a) shows variation in the onset shear strain at localization with a confining pressure for two void ratios, $e_0 = 0.7$ and 0.65. The effect of confining pressure on shear-band orientation is presented in Fig. 7(b), which also depicts an

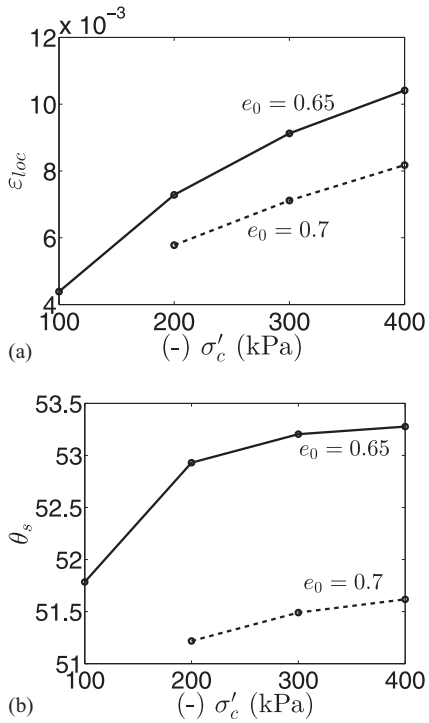

Fig. 7. Effect of initial effective confining pressure (σ_c') on (a) shear strain at localization (ε_{loc}) and (b) band angle inclination (θ_s) for two void ratios

increasing trend with an increase in the initial effective confining pressure. Finno et al. (1997), Mooney et al. (1997), and Mokni and Desrues (1998) experimentally reported a similar trend in the orientation of shear band with an increase in the initial effective confining pressure during undrained testing of saturated sand.

Friction and Dilatancy Angles at Onset of Instability

The evolution of friction and dilatancy angles is plotted in Fig. 8 for $e_0 = 0.65$ and 0.85 with varying confining stress. The instability onsets in the rigid boundary are also shown in the plot. In all of these cases, both SF and localization-type instabilities occurred before the stage when the friction or dilation angles reached their peak. Moreover, the friction and dilatancy angles at the onset of instability were observed

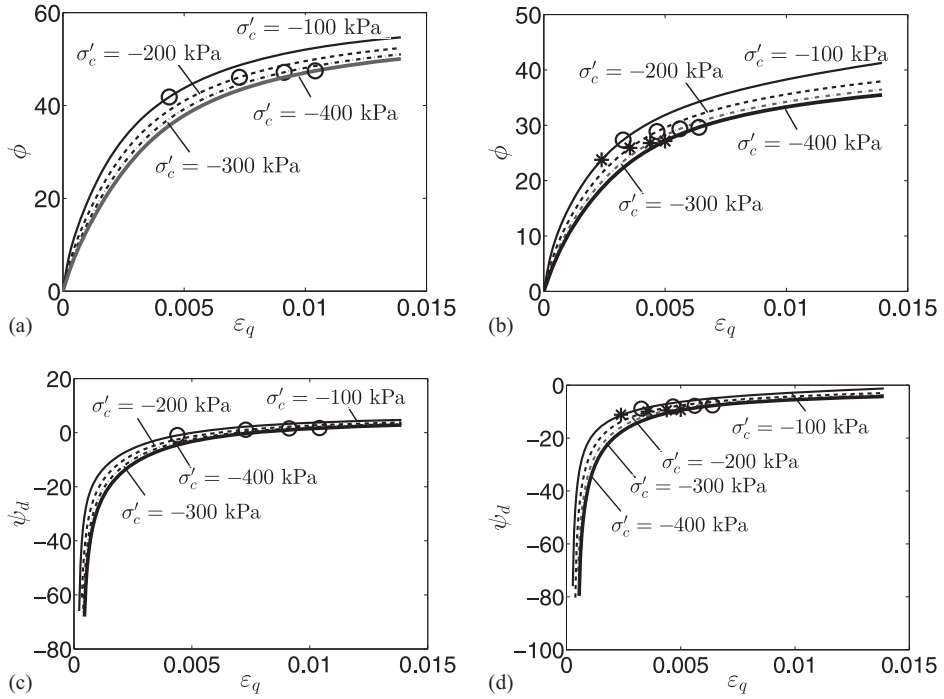

Fig. 8. Evolution of (a and b) friction angle (ϕ) and (c and d) dilatancy angle (ψ_d) for $e_0 = 0.65$ and 0.85 with various initial effective confining pressures

to increase with increasing confinement. In the case of dense sands, localization emerged near the limit of zero volume change, resulting in a small positive dilation angle at localization. Han and Vardoulakis (1991) and Finno et al. (1997) also observed that the localization takes place before the peak friction angle is achieved.

Shear-band angles for the two-dimensional plane-strain problem are often calculated using the following relations as a function of the friction angle (ϕ) and dilatancy angle (ψ_d) at the onset of localization:

Mohr–Coulomb theory: $\theta_{CM} = \frac{\pi}{4} + \frac{\phi}{2}$

Roscoe theory: $\theta_{CR} = \frac{\pi}{4} + \frac{\psi_d}{2}$

Arthur et al. (1977):

$$\theta_{CA} = \frac{\pi}{4} + \frac{\phi}{4} + \frac{\psi_d}{4} \tag{18}$$

Inclination of shear bands was calculated for dense sand with $e_0 = 0.65$ at various confining pressures using the relations from Eq. (18), which are depicted in Fig. 9. For all of these cases, the values of θ_{CA} were lower and θ_{CM} were significantly higher than the localization angle (θ_b) calculated from the bifurcation analysis. The values of θ_{CA} were also on the slightly higher side, but within 2–3° of difference. Similar to the bifurcation solution, the band angles calculated from these relations implied an increasing trend with an increase in the initial confining pressure.

Charts for Instability Onset

The effect of void ratio and initial effective confining pressure on the emergence of possible instability modes in the rigid boundary

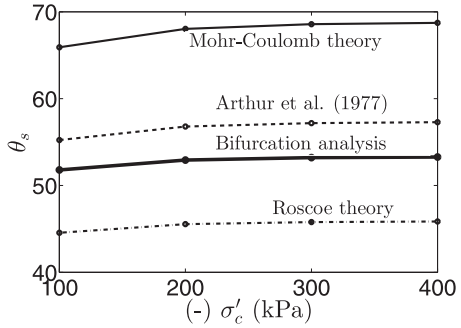

Fig. 9. Effect of initial effective confining pressure (σ'_c) on inclination of shear-band angle (θ_s) calculated from Eq. (18)

are further evaluated in this section. The state variable was used as a parameter to characterize the instability response. The state variable (ψ) represents relative density of sand in some sense and includes the effect of both initial density and confining pressure. A negative value of the initial state variable (ψ_0) implies a denser state, whereas a positive value indicates loose state. Fig. 10 presents the evolution of the two-phase instability coefficient and normalized critical hardening modulus associated with localization with the parameter ψ_0 for the case simulated at $e_0 = 0.73$ and varying initial confining pressure from 100 to 400 kPa. The onset shear strains for the two-phase and localized instability modes were determined by following the procedure mentioned in Appendixes II and III and is replotted in Fig. 10(c) against ψ_0. The density varied form loose to a denser state as ψ_0 changed from –0.1 to –0.06. SF instability preceded the localization mode at loose states with $\psi_0 \leq -0.08$, after which only localization-type instability was observed.

The onset shear strains for these two types of instabilities are presented using contour plots in Fig. 11. The instability onsets were obtained by varying the void ratio from 0.65 to 0.85 over

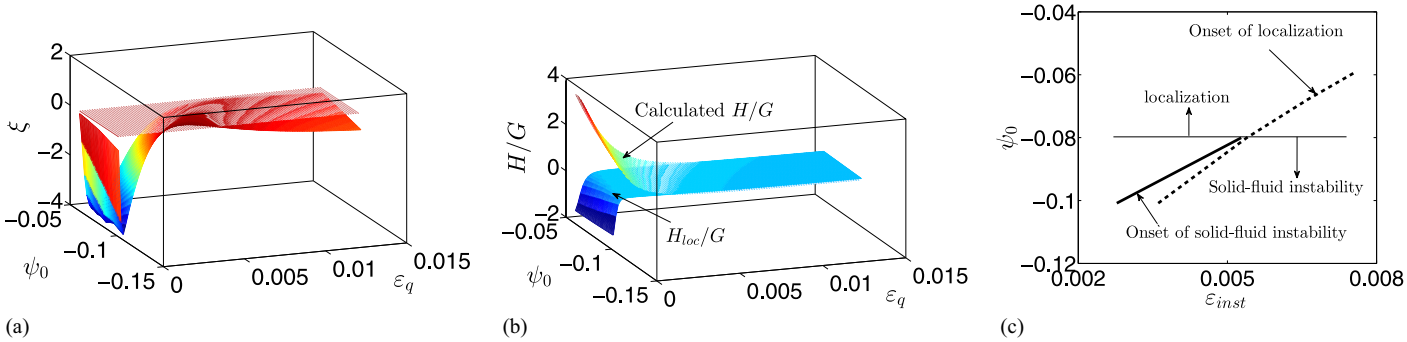

Fig. 10. Evolution of (a) two-phase instability coefficient ($\xi = b^2 - 4c$), (b) calculated (H/G) and critical (H_{loc}/G) normalized hardening modulus for localization, and (c) onset shear strains (ε_{inst}) of two types of instability modes with parameter ψ_0 for $e_0 = 0.73$ and initial effective confining pressures ranging from 100 to 400 kPa

the initial effective confining pressure range of 100–400 kPa. Figs. 11(a and c) present the contours of SF instability modes along with the critical state line (CSL), characterized by $\psi = 0$. It can observed from Fig. 11(a) that the onset shear strain for such instability was a function of both void ratio and confining pressure. As noticed in an earlier section, the onset strain increased with the decrease in void ratio and increasing initial confining pressure. However, the increasing slope of these contours indicates a larger impact of void ratio at higher confinement compared to the lower ones. This can further be analyzed from Fig. 11(c), where the contours were replotted against ψ_0 and confining pressure. The onset strains were not uniquely related to ψ_0 and showed significant dependence on confining pressure along with ψ_0. The slope of these contours reduced with an increase in the confining pressure, implying more pronounced effect of confinement at a lower range of confining pressure, whereas at a higher confining pressure, the influence of ψ_0 was induced mainly through void ratio. The slope and spacing of such contours were different at two sides of the CSL. The spacing in Fig. 11(a) was much larger on the right side of the CSL, implying a higher influence of void ratio and confining pressure at the loose state.

The contour plots of onset shear strains for localization instability are presented in Figs. 11(b) and 11(d). The strain contours in Fig. 11(b) are nearly perpendicular to the CSL, and the radial contours indicate a larger impact of void ratio and confining pressure at higher void ratios and confinement. However, the influence of confining pressure decreases with an increasing level of confinement, which is evident from the gradually reducing contour slopes of Fig. 11(d). It is important to note that SF instability is the dominating mode at higher void ratios and confinement, which can even be followed by strain localization phenomena. Hence, in this region, the strain contours for localization onset, as predicted from a homogeneous stress-strain field, do not represent the actual scenario and require a proper postbifurcation analysis through appropriate FEM simulation. The material model used here for the biaxial instability analysis does not capture the Lode angle effect that is often observed in soils. However, this is not a concern in the applicability of these charts in general, because the Lode angle does not vary significantly during plane-strain shearing (Vardoulakis 1980).

Two-Phase Instability Line in Stress Space

The two-phase instability line in stress space is defined by joining the points of peak shear stress from a series of undrained tests to the origin of the stress space (Lade 1992). The slope of the two-phase instability line or instability angle is nonunique and depends on initial relative density (i.e., more specifically, void ratio and confining pressure at the start of undrained shearing) (Lade 1993; Yamamuro and Lade 1997). In a series of undrained triaxial experiments on Nevada sand, Yamamuro and Lade (1997) noticed the instability angle remained constant at higher relative densities, but increased with initial confining pressure at lower densities, whereas a decreasing instability angle was observed with the initial void ratio before shearing. Chu et al. (2003) and Wanatowski and Chu (2007) also observed a reduction in the slope of the instability line with initial void ratio before shearing during the undrained plane-strain test on marine sand. Here, instability angles were calculated by joining the two-phase instability point in the rigid boundary and the origin of stress space, and its variation with initial void ratio and confining pressure is plotted in Fig. 12. The observations are consistent with the previous literature. The influence of confining pressure on instability line was more significant at lower void ratios and reduced with a higher level of confinement.

Conclusions

The emergence of two types of instability modes (i.e., SF and strain localization) has been assessed for undrained biaxial tests on sand with both flexible and rigid lateral boundaries. A large deformation–based plane-strain bifurcation analysis was performed to examine the possibility of these instability modes at different densities, confining pressures, and the applied boundary conditions. The material was assumed to follow the rate-independent 3D nonassociative constitutive law of Wood (2004) to capture most of the undrained instability modes at different states of material and boundary conditions. The existing analytical framework for predicting two-phase instability under a rigid lateral boundary was extended to laterally flexible conditions to look into the effect of boundary condition on undrained instability modes. The onset of two-phase instabilities under undrained biaxial loading with a flexible lateral boundary was thus analyzed theoretically for the first time in this study. The instability predictions were found to be qualitatively in good agreement with the experimental observations. The onset of undrained instabilities from small deformation analysis overlapped with that from the large deformation formulation.

The SF instability modes were found to be more crucial for loose to medium-dense sands, which emerged just before the peak shear

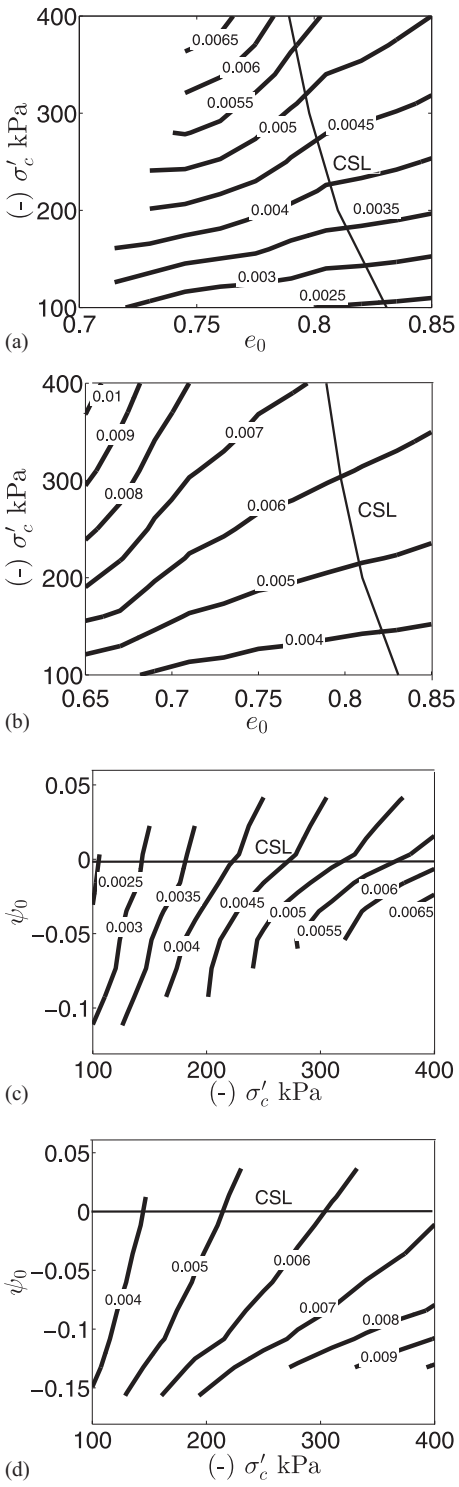

Fig. 11. Contours of onset shear strain with (a and b) void ratio e_0 and initial effective confining pressure (σ_c') and (c and d) ψ_0 and initial effective confining pressure for SF and localization instability, respectively

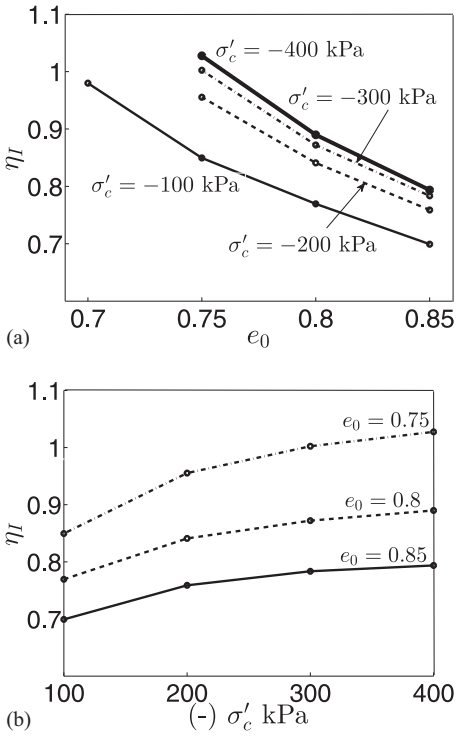

Fig. 12. Effect of (a) void ratio (e_0) and (b) initial effective confining pressure (σ_c') on slope of instability line (η_I)

stress under biaxial loading with the rigid lateral boundary, whereas emergence of such modes was delayed significantly in the case of the flexible boundary. The localized deformation modes preceded the two-phase instability modes in the flexible boundary case, unlike the rigid boundary case. Hence, loose-sand samples may not undergo SF instability or static liquefaction in such test configurations, and the localized type of instabilities are more likely to take place in these cases. These results are consistent with the experimental observations by Han and Vardoulakis (1991), Finno et al. (1997), and Mooney et al. (1997) on loose sand under laterally flexible undrained biaxial testing. For dense sand, localization-type modes were the primary instability mode under both boundary conditions.

The onset of both SF instability and localized mode was retarded by an increase in the initial effective confining pressure and a decrease in void ratio. In the case of medium-dense sand, two-phase instability modes were activated only at lower confinements with a clear phase change. An increasing trend was noted in the inclination of the shear-band angle with increasing initial confining pressure. The charts of instability onset showed that the confining pressure and void ratio both had strong influence in emergence of instabilities at different magnitudes of these variables. In a similar way, the slope of the two-phase instability line in stress space was also found to be a function of both the initial void ratio and the confining pressure before undrained shearing.

Appendix I. SF Instability Modes under Flexible Lateral Boundary

The mathematical formulation for analyzing two-phase or SF instability modes under flexible lateral boundary conditions is derived in this appendix. The derived equations do not appear in the existing literature. Two-phase or SF instability modes, which can emerge during undrained loading of a saturated soil specimen, should satisfy the stress rate equilibrium equation given in Eq. (4) and the boundary conditions considered in Eqs. (5) and (6). For biaxial loading, the general expression for the perturbed velocity field associated with the two-phase instability can be represented by

$$v_1 = V_1 \sin(\gamma_1 x_1 + \theta_1)\cos(\beta_2 x_2 + \theta_2) f(t)$$
$$v_2 = V_2 \cos(\gamma_1 x_1 + \theta_1)\sin(\beta_2 x_2 + \theta_2) f(t)$$
$$\dot{p} = P \cos(\beta_1 x_1 + \theta_1)\cos(\beta_2 x_2 + \theta_2) f(t) \tag{19}$$

where V_1, V_2, and P = arbitrary modal amplitudes; and $f(t)$ = unknown function of time. The assumed velocity modes satisfy the boundary conditions of Eqs. (5) and (6) provided the coefficients β_1, β_2, θ_1, and θ_2 are selected as follows:

$$\beta_1 L_1 = \frac{\pi}{2} m_1 \quad \text{for} \quad m_1 = \pm 1, \pm 2, \ldots$$
$$\beta_2 L_2 = \frac{\pi}{2} m_2 \quad \text{for} \quad m_2 = \pm 1, \pm 2, \ldots$$
$$\theta_1 = \begin{cases} 0 & \text{for } m_1 \text{ even} \\ \frac{\pi}{2} & \text{for } m_1 \text{ odd} \end{cases} \quad \text{and} \quad \theta_2 = \begin{cases} 0 & \text{for } m_2 \text{ even} \\ \frac{\pi}{2} & \text{for } m_2 \text{ odd} \end{cases} \tag{20}$$

where m_1 and m_2 = arbitrary integers. In the case of the flexible boundary (Case 1), the boundary condition at $x_1 = \pm L_1$ and $-L_2 \le x_2 \le L_2$ requires $\gamma_1 L_1 \ne m_3 \pi/2$ for an arbitrary integer $m_3 = \pm 1, \pm 2 \ldots$ and

$$d_1 \gamma_1 V_1 + d_7 \beta_2 V_2 = 0$$
$$d_4 \beta_2 V_1 + d_5 \gamma_1 V_2 = 0 \tag{21}$$

For nontrivial V_1 and V_2, determinant of simultaneous Eq. (21) should be zero, which leads to the relation

$$d_1 d_5 \gamma_1^2 - d_4 d_7 \beta_2^2 = 0 \tag{22}$$

Substituting the perturbed velocity fields of Eq. (19) into Eq. (4) gives

$$(d_1 \gamma_1^2 + d_3 \beta_2^2) V_1 l_1 + (d_4 + d_7) \gamma_1 \beta_2 V_2 l_1 - \beta_1 P l_3 = 0$$
$$(d_4 + d_8) \gamma_1 \beta_2 V_1 l_2 + (d_5 \gamma_1^2 + d_2 \beta_2^2) V_2 l_2 - \beta_2 P l_4 = 0$$
$$\gamma_1 \bar{f}^* V_1 \frac{l_2}{l_4} + \beta_2 \bar{f}^* V_2 \frac{l_2}{l_4} + (\beta_1^2 + \beta_2^2) P = 0$$
$$\text{where } l_1 = \sin(\gamma_1 x_1 + \theta_1), l_2 = \cos(\gamma_1 x_1 + \theta_1)$$
$$l_3 = \sin(\beta_1 x_1 + \theta_1), l_4 = \cos(\beta_1 x_1 + \theta_1) \tag{23}$$

The coefficient $\bar{f}^*$ is defined as

$$\bar{f}^* = \frac{b\dot{f}(t)}{f(t)} = -\frac{(\beta_1^2 + \beta_2^2) P}{(\gamma_1 V_1 + \beta_2 V_2)} \frac{l_4}{l_2} \tag{24}$$

The coefficient $\bar{f}^*$ is independent of time; however, it depends on spatial coordiate x_1. The solution to Eq. (24) is $f(t) = f_0 \exp(\bar{f}^* t/b)$, where f_0 represents the initial amplitude of a perturbation of the trivial solution of Eq. (4) and the exponential rate of growth or decay of $f(t)$ is $(\bar{f}^* t/b)$. In the case of $\bar{f}^* > 0, f$ grows exponentially with time, and eventually becomes infinite, whereas when $\bar{f}^* < 0$, the initial perturbation dies out with time. Hence, the mode considered in Eq. (19) is stable when $\bar{f}^* < 0$ and unstable when $\bar{f}^* > 0$. The growth of perturbation with time [i.e., $f(t)$] varies with x_1 and so is the onset condition for SF instability, which can be derived by equating the determinant of Eq. (23) to zero for ensuring nontrivial solution of V_1, V_2, and P

$$\frac{\bar{f}^*}{\beta_1^2 + \beta_2^2} = \frac{\bar{N}(\gamma_1, \beta_2)}{\bar{G}(\gamma_1, \beta_1, \beta_2)} \tag{25}$$

where

$$\bar{N} = d_1 d_5 \gamma_1^4 + d_2 d_3 \beta_2^4 + \gamma_1^2 \beta_2^2 \{d_1 d_2 + d_3 d_5 + (d_4 + d_7)(d_4 + d_8)\}$$
$$\bar{G} = (d_4 + d_7) \gamma_1^2 \beta_2^2 - \beta_2^2 (d_1 \gamma_1^2 + d_3 \beta_2^2) + \frac{l_2}{l_1} \frac{l_3}{l_4} \{(d_4 + d_8) \gamma_1 \beta_1 \beta_2^2 - (d_5 \gamma_1^2 + d_2 \beta_2^2) \gamma_1 \beta_1\} \tag{26}$$

This equation is defined within the domain $-L_1 \le x_1 \le L_1$, except at $x_1 = 0$. SF mode emerges for the condition $\bar{f}^* > 0$ (i.e., $\bar{N}/\bar{G} > 0$), whereas an infinite exponential growth ($f^* \to +\infty$) occurs for SF instability (SF∞) modes when $\bar{G} = 0$ and $\bar{N} \ne 0$.

S instability modes under globally undrained conditions can also be explored within the present bifurcation framework. Eq. (25) is further simplified to the following form using Eq. (24):

$$\frac{P}{(\gamma_1 V_1 + \beta_2 V_2)} \frac{\cos(\beta_1 x_1 + \theta_1)}{\cos(\gamma_1 x_1 + \theta_1)} = \frac{\bar{N}}{\bar{G}} \tag{27}$$

S instability mode (i.e., nontrivial V_i and $P = 0$) can be obtained in the flexible boundary condition provided Eq. (27) is satisfied by having $\bar{N} = 0$. For the flexible boundary, S instability modes can emerge in the form of either strain localization or diffused instability modes. The restriction ($P = 0$) requires assumption of locally drained conditions for emergence of such S instabilities under globally undrained biaxial loading. This assumption can be reasonable for the case of strain localization or shear bands where only a small zone of intense shearing is involved. However, such an assumption is not justified for diffused instabilities that involve a larger volume of soil sample with local internal drainage resulting in local volume change and nonuniform pore pressure distribution. A finite-element–based analysis may help in this regard. In the present study, the focus was restricted only to the localized type of S instabilities.

Appendix II. SF Modes under Rigid Lateral Boundary

For the biaxial loading with rigid boundary (Case 2), two-phase instability modes can be represented by the perturbed velocity field of Eq. (19) provided $\gamma_1 = \beta_1$ to satisfy Eq. (6). After substituting this modified velocity field, the governing equations for the rigid boundary can still be represented by Eq. (23) with $l_1 = l_2 = l_3 = l_4 = 1$ and $\bar{f}^*$ replaced by f^*. The expression for coefficient f^* is the same as defined by Eqs. (30) and (32) in Bardet and Shiv (1995), which were previously derived for detecting SF instability under biaxial loading with rigid boundaries and incompressible pore fluid. In this case, the coefficient f^* is independent of time and space, and the growth of perturbation with time [i.e., $f(t) = f_0 \exp(f^* t/b)$] does not depend on the spatial coordinate. Similar to the flexible

boundary case, the SF instability mode with wavelength ratio $\Lambda = \beta_1/\beta_2$ emerges when $f^* > 0$ [i.e., $N(\Lambda)/G_r(\Lambda) > 0$, where $N = a_1\Lambda^4 + b_1\Lambda^2 + c_1$; and $G_r = a_2\Lambda^4 + b_2\Lambda^2 + c_2$. The coefficients a_1, b_1, c_1, a_2, b_2, and c_2 are

$$a_1 = d_1 d_5\,,\ b_1 = d_1 d_2 + d_3 d_5 - (d_4 + d_7)(d_4 + d_8)\,,\ c_1 = d_2 d_3$$
$$a_2 = -d_5\,,\ b_2 = -(d_1 + d_2 - 2d_4 - d_7 - d_8)\,,\ c_2 = -d_3 \tag{28}$$

whereas SF∞ instability is encountered for the condition $G_r = 0$ and $N \neq 0$. In the case of incompressible pore fluid, the condition for SF∞ mode requires $\Lambda = -V_2/V_1$ (Bardet and Shiv 1995; Iai and Bardet 2001). The condition for emergence of SF∞ mode can be rewritten as

$$G_r = \Lambda^4 + b\Lambda^2 + c = 0 \tag{29}$$

where

$$b = \frac{d_1 + d_2 - 2d_4 - d_7 - d_8}{d_5} \quad \text{and} \quad c = \frac{d_3}{d_5} \tag{30}$$

To get a real solution for Λ, the following condition should be satisfied at the onset of SF∞ instability:

$$b^2 - 4c \geq 0 \quad \text{and} \quad b < 0 \tag{31}$$

A pure S instability mode under rigid boundaries requires $N = 0$. The rigid boundary condition imposed by Eq. (6) restricts the occurrence of diffused instability modes and allows only localized shear bands to generate. It is important to note that the S instability conditions for both the rigid and flexible case (i.e., $N = 0$ and $\bar{N} = 0$) refer to the same characteristic equation in terms of β_1 and β_2 or γ_1 and β_2. The governing equations related to the localization type of instability mode are discussed in the subsequent section.

Appendix III. Solid Instability Mode in Form of Localization

The localized type of solid instability mode arises when a nonhomogeneous velocity field ($\mathbf{v}$) emerges in a planar region in the form of shear bands. A globally undrained but locally drained condition has been assumed to identify the onset condition for localized modes. The velocity continuity for such a case requires $[\![v_{i,j}]\!] = g_i n_j$, where $[\![\,]\!]$ denotes the jump or difference in magnitude of the field variable within and outside the band. The normal vectors $\mathbf{n}$ and $\mathbf{g}$ are arbitrary vectors that depend only on the distance across the band and vanish outside the band. Here, the kinematic constraint due to plane-strain conditions is satisfied when $[\![D_{33}]\!] = [\![D_{13}]\!] = [\![D_{23}]\!] = 0$, which further results in $g_3 = n_3 = 0$. The equilibrium of stress rate across the shear band is enforced by the relation $n_j[\![\dot{S}_{ji}]\!] = 0$. The condition for the nontrivial solution of g_1 and g_2 can be obtained by substituting the velocity continuity relation into the equilibrium equation, which leads to the same characteristic equation for both rigid and flexible cases (i.e., $N = 0$ or $\bar{N} = 0$) (Rice 1976; Bardet 1991). Based on the coefficients a_1, b_1, and c_1, the characteristic equation can have either four or two real roots, depending on whether it is hyperbolic or parabolic in nature, respectively. For the hyperbolic regime (i.e., $\zeta = b_1^2 - 4a_1c_1 \geq 0$, $b_1/a_1 \geq 0$, $c_1/a_1 \geq 0$), the solutions are

$$n_1, n_2 = \pm\sqrt{\frac{-b_1 - \sqrt{\zeta}}{2a_1}}\,,\ n_3, n_4 = \pm\sqrt{\frac{-b_1 + \sqrt{\zeta}}{2a_1}} \tag{32}$$

whereas for the parabolic regime (i.e., $c_1/a_1 < 0$), the solutions are given by

$$n_1, n_2 = \pm\sqrt{\max\left(\frac{-b_1 - \sqrt{\zeta}}{2a_1}, \frac{-b_1 + \sqrt{\zeta}}{2a_1}\right)} \tag{33}$$

Such localized modes are first available on the elliptic/hyperbolic boundary ($\zeta = 0$) with only two unique roots. The shear-band angle (θ_s) from the lateral direction (i.e., clockwise from the x_1-axis) can be calculated by using the relation $n_1 = \sin\theta_s$ and $n_2 = \cos\theta_s$.

References

Alshibli, K. A., Batiste, S. N., and Sture, S. (2003). "Strain localization in sand: Plane strain versus triaxial compression." *J. Geotech. Geoenviron. Eng.*, 10.1061/(ASCE)1090-0241(2003)129:6(483), 483–494.

Arthur, J. F. R., Dunstan, T., Assadi, Q. A. J., and Assadi, A. (1977). "Plastic deformation and failure in granular media." *Géotechnique*, 27(1), 53–74.

Bardet, J. P. (1991). "Analytical solutions for the plane-strain bifurcation of compressible solids." *J. Appl. Mech.*, 58(3), 651–657.

Bardet, J. P., and Shiv, A. (1995). "Plane-strain instability of saturated porous media." *J. Eng. Mech.*, 10.1061/(ASCE)0733-9399(1995)121:6(717), 717–724.

Bigoni, D. (2000). "Bifurcation and instability of nonassociative elasticplastic solids." *Material Instabilities in Elastic and Plastic Solids, CISM Lecture Notes No.414*, H. Petryk, ed., Springer-Verlag, New York, 1–52.

Bigoni, D., and Hueckel, T. (1991). "Uniqueness and localization—I. Associative and non-associative elastoplasticity." *Int. J. Solids Struct.*, 28(2), 197–213.

Borja, R. I. (2006). "Condition for liquefaction instability in fluid-saturated granular soils." *Acta Geotech.*, 1(4), 211–224.

Chau, K. T., and Rudnicki, J. W. (1990). "Bifurcation of compressible pressure-sensitive materials in plane strain tension and compression." *J. Mech. Phys. Solids*, 38(6), 875–898.

Chu, J., Leroueil, S., and Leong, W. K. (2003). "Unstable behaviour of sand and its implication for slope stability." *Can. Geotech. J.*, 40(5), 873–885.

Chu, J., and Wanatowski, D. (2008). "Instability conditions of loose sand in plane strain." *J. Geotech. Geoenviron. Eng.*, 10.1061/(ASCE)1090-0241(2008)134:1(136), 136–142.

Daouadji, A., AlGali, H., Darve, F., and Zeghloul, A. (2010). "Instability in granular materials: Experimental evidence of diffuse mode of failure for loose sands." *J. Eng. Mech.*, 10.1061/(ASCE)EM.1943-7889.0000101, 575–588.

Daouadji, A., et al. (2011). "Diffuse failure in geomaterials: Experiments, theory and modelling." *Int. J. Numer. Anal. Methods Geomech.*, 35(16), 1731–1773.

Desai, C. S., and Siriwardane, H. J. (1984). *Constitutive laws for engineering materials, with emphasis on geologic materials*, Prentice-Hall, Upper Saddle River, NJ.

Desrues, J., and Georgopoulos, I. O. (2006). "An investigation of diffuse failure modes in undrained triaxial tests on loose sand." *Soils Found.*, 46(5), 585–594.

Desrues, J., and Hammad, W. (1989). "Shear banding dependency on mean stress level in sand." *2nd Int. Workshop on Numerical Methods for Localization and Bifurcation of Granular Bodies, Gdansk-Karlsruhe*, E. Dembicki, G. Gudehus, and Z. Sikora, eds., Technical Univ. of Gdansk, Gdansk, Poland, 57–67.

Desrues, J., Lanier, J., and Stutz, P. (1985). "Localization of the deformation in tests on sand sample." *Eng. Fract. Mech.*, 21(4), 909–921.

Desrues, J., and Viggiani, G. (2004). "Strain localization in sand: An overview of the experimental results obtained in grenoble using stereophotogrammetry." *Int. J. Numer. Anal. Methods Geomech.*, 28(4), 279–321.

Dodds, R. H., and Healy, B. E. (2001). "A large strain plasticity model for implicit finite element analyses". *Rep. No. UILU-ENG-91-2001*, Univ. of Illinois at Urbana-Champaign, Dept. of Civil Engineering, Urbana, IL.

Einav, I., and Puzrin, A. M. (2004). "Pressure-dependent elasticity and energy conservation in elastoplastic models for soils." *J. Geotech. Geoenviron. Eng.*, 10.1061/(ASCE)1090-0241(2004)130:1(81), 81–92.

Finno, R. J., Harris, W. W., Mooney, M. A., and Viggiani, G. (1997). "Shear bands in plane strain compression of loose sand." *Géotechnique*, 47(1), 149–165.
Finno, R. J., Harris, W. W., Mooney, M. A., and Viggiani, G. (1996). "Strain localization and undrained steady state of sand." *J. Geotech. Eng.*, 10.1061/(ASCE)0733-9410(1996)122:6(462), 462–473.
Gajo, A., Bigoni, D., and Wood, D. M. (2004). "Multiple shear band development and related instabilities in granular materials." *J. Mech. Phys. Solids*, 52(12), 2683–2724.
Gajo, A., and Wood, D. M. (1999). "A kinematic hardening constitutive model for sands: The multiaxial formulation." *Int. J. Numer. Anal. Methods Geomech.*, 23(9), 925–965.
Gajo, A., Wood, D. M., and Bigoni, D. (2007). "On certain critical material and testing characteristics affecting shear band development in sand." *Géotechnique*, 57(5), 449–461.
Guo, P. (2013). "Undrained shear band in water saturated granular media: A critical revisiting with numerical examples." *Int. J. Numer. Anal. Methods Geomech.*, 37(4), 353–373.
Guo, P., and Stolle, D. F. E. (2013). "Coupled analysis of bifurcation and shear band in saturated soils." *Soils Found.*, 53(4), 525–539.
Han, C., and Vardoulakis, I. (1991). "Plane strain compression experiments on water saturated fine grained sand." *Géotechnique*, 41(1), 49–78.
Hardin, B. O., and Black, W. L. (1966). "Sand stiffness under various triaxial stresses." *J. Soil Mech. Found. Eng. Div.*, 91(SM2), 353–369.
Hicher, P. Y. (1996). "Elastic properties of soils." *J. Geotech. Eng.*, 10.1061/(ASCE)0733-9410(1996)122:8(641), 641–648.
Hill, R. (1958). "A general theory of uniqueness and stability in elastic-plastic solids." *J. Mech. Phys. Solids*, 6(3), 236–249.
Hill, R. (1961). "Bifurcation and uniqueness in non-linear mechanics of continua." Prob. Continuum Mech., 155–164. S.I.A.M., J. R. M. Radok, ed, Society for Industrial and Applied Mathematics, Philadelphia.
Hill, R., and Hutchinson, J. W. (1975). "Bifurcation phenomena in the plane tension test." *J. Mech. Phys. Solids*, 23(4–5), 239–264.
Houlsby, G. T., Amorosi, A., and Rojas, E. (2005). "Elastic moduli of soils dependent on pressure: A hyperelastic formulation." *Géotechnique*, 55(5), 383–392.
Iai, S., and Bardet, J. P. (2001). "Plane strain instability of saturated elastoplastic soils." *Géotechnique*, 51(5), 389–398.
Khoa, H., Georgopoulos, I., Darve, F., and Laouafa, F. (2006). "Diffuse failure in geomaterials: Experiments and modelling." *Comput. Geotech.*, 33(1), 1–14.
Lade, P. V. (1992). "Static instability and liquefaction of loose fine sandy slopes." *J. Geotech. Eng.*, 10.1061/(ASCE)0733-9410(1992)118:1(51), 51–71.
Lade, P. V. (1993). "Initiation of static instability in the submarine nerlerk berm." *Can. Geotech. J.*, 30(6), 895–904.
Lade, P. V. (2002). "Instability, shear banding, and failure in granular materials." *Int. J. Solids Struct.*, 39(13–14), 3337–3357.
Lade, P. V., and Nelson, R. B. (1987). "Modelling the elastic behaviour of granular materials." *Int. J. Numer. Anal. Methods Geomech.*, 11(5), 521–542.
Lade, P. V., and Pradel, D. (1990). "Instability and plastic flow of soils. I: Experimental observations." *J. Eng. Mech.*, 10.1061/(ASCE)0733-9399(1990)116:11(2532), 2532–2550.
Lade, P. V., and Yamamuro, J. A. (1997). "Effects of non-plastic fines on static liquefaction of sands." *Can. Geotech. J.*, 34(6), 918–928.
Mokni, M., and Desrues, J. (1998). "Strain localization measurements in undrained plane-strain biaxial tests on Hostun RF sand." *Mech. Cohesive-Frict. Mater.*, 4, 419–441.
Mooney, M. A., Viggiani, G., and Finno, R. J. (1997). "Undrained shear band deformation in granular media." *J. Eng. Mech.*, 10.1061/(ASCE)0733-9399(1997)123:6(577), 577–585.
Needleman, A. (1979). "Non-normality and bifurcation in plane-strain tension and compression." *J. Mech. Phys. Solids*, 27(3), 231–254.
Rice, J. R. (1976). "The localization of plastic deformation." *Proc., 14th Int. Congress on Theoretical and Applied Mechanics*, Vol. 1, North-Holland Publishing, Amsterdam, Netherlands, 207–220.
Schrefler, B. A., Simoni, L., Xikui, L., and Zienkiewicz, O. C. (1990). "Mechanics of partially saturated porous media." *Numerical methods and constitutive modeling in geomechanics*, C. S. Desai and G. Gioda, eds., Springer-Verlag, New York, 169–209.
Simo, J. C., and Hughes, T. J. R. (2000). *Computational inelasticity*, Springer, New York.
Terzaghi, K. V. (1943). *Theoretical soil mechanics*, John Wiley and Sons, New York.
Vardoulakis, I. (1980). "Shear band inclination and shear modulus of sand in biaxial tests." *Int. J. Numer. Anal. Methods Geomech.*, 4(2), 103–119.
Vardoulakis, I. (1981). "Bifurcation analysis of the plane rectilinear deformation on dry sand samples." *Int. J. Solids Struct.*, 17(11), 1085–1101.
Vardoulakis, I. (1985). "Stability and bifurcation of undrained, plane rectilinear deformations on water-saturated granular soils." *Int. J. Numer. Anal. Methods Geomech.*, 9(5), 399–414.
Vardoulakis, I. (1996a). "Deformation of water-saturated sand: I. Uniform undrained deformation and shear banding." *Géotechnique*, 46(3), 441–456.
Vardoulakis, I. (1996b). "Deformation of water-saturated sand: II. Effect of pore water flow and shear banding." *Géotechnique*, 46(3), 457–472.
Wan, R., Pinheiro, M., Daouadji, A., Jrad, M., and Darve, F. (2013). "Diffuse instabilities with transition to localization in loose granular materials." *Int. J. Numer. Anal. Methods Geomech.*, 37(10), 1292–1311.
Wanatowski, D., and Chu, J. (2007). "Static liquefaction of sand in plane strain." *Can. Geotech. J.*, 44(3), 299–313.
Wood, D. M. (2004). *Geotechnical modeling*, CRC Press, Boca Raton, FL.
Yamamuro, J. A., and Lade, P. V. (1997). "Static liquefaction of very loose sands." *Can. Geotech. J.*, 34(6), 905–917.
Young, N. J. B. (1976). "Bifurcation phenomena in plane compression test." *J. Mech. Phys. Solids*, 24(1), 77–91.